

# Enhanced Corrosion Resistance and Photocatalytic Properties of Bi<sub>2</sub>O<sub>3</sub>/Phosphate Composite Film Prepared on AZ91D Magnesium Alloy by Phosphating

Dong Liu<sup>1,2,3</sup>, Junchao Huang<sup>1</sup>, Yong Zhou<sup>2</sup> and Yigang Ding<sup>2,\*</sup>

<sup>1</sup> School of Chemistry and Environmental Engineering, Wuhan Institute of Technology, Wuhan 430205, China; liudong1980@aliyun.com (L.D.); h2715478468@126.com (H.J.)

<sup>2</sup> Key Lab for Green Chemical Process of Ministry of Education, Wuhan Institute of Technology, Wuhan 430205, China; zhouyong@wit.edu.cn (Z.Y.)

<sup>3</sup> State Key Laboratory of Oil and Gas Reservoir Geology and Exploitation, Southwest Petroleum University, Chengdu 610500, China

\*E-mail: [dingyg2016@163.com](mailto:dingyg2016@163.com)

Received: 9 November 2019 / Accepted: 14 December 2018 / Published: 5 January 2019

---

A Bi<sub>2</sub>O<sub>3</sub>/phosphate composite film was prepared on AZ91D magnesium alloy by phosphate treatment. The surface morphology, chemical composition and corrosion resistance of the composite film were investigated by SEM, EDS, XPS and electrochemical measurements. Meanwhile, the wettability of the composite film was examined by contact angle measurements. The results showed that the composite film was mainly composed of CaHPO<sub>4</sub> and Bi<sub>2</sub>O<sub>3</sub>, and the thickness of the film was approximately 15 μm. The corrosion current density of the Bi<sub>2</sub>O<sub>3</sub>/phosphate composite film-coated sample was 100 times lower than that of bare AZ91D. Immersion tests conducted in ASTM D1384-87 solution demonstrated the durability of the composite film-coated AZ91D. Furthermore, the composite film possessed photocatalytic activity, which could protect Mg alloy from corrosion by atmospheric pollutants.

---

**Keywords:** AZ91D magnesium alloy; phosphating treatment; Bi<sub>2</sub>O<sub>3</sub>; corrosion resistance; photocatalytic performance

## 1. INTRODUCTION

Due to its low density, high strength/weight ratio, good machinability and excellent recyclability, magnesium (Mg) and its alloys are increasingly used in various industries, including transportation, communication and personal electronics [1-3]. However, the high chemical reactivity of Mg and its alloys makes them susceptible to corrosion in different environments [4-6]. As structural materials, Mg

and its alloys are mostly applied in atmospheric environments. Hence, the atmospheric corrosion of Mg alloys has become a heavily researched topic. In addition, some pollutants in the atmosphere could accumulate on the surface of the magnesium alloy, which causes a more serious problem of corrosion. As reported, atmospheric pollution can accelerate the degradation of metal materials and, whilst this may shorten the service life of certain structures, it more generally means that additional costs have to be met for structural maintenance.

Phosphate treatment is a common and important surface protection technology for magnesium alloy [7]. A protective phosphate film can be deposited on the surface of magnesium alloy through phosphating. Generally, phosphate film is applied for two reasons [8, 9]. Phosphate film can be used as a transition layer to improve the bonding strength between the organic coating and the magnesium alloy matrix. Alternatively, phosphate film can provide protection against corrosion to magnesium alloy in the atmosphere or in a corrosive electrolyte environment. However, the protective effect of the phosphate film on magnesium alloy is limited [10, 11]. Therefore, organic or inorganic additives are usually added to the phosphating treatment solution to enhance the protective effect of the phosphate film [12-16]. In the field of modification with organic additives, studies on SDBS, MEA and SMBS have been widely reported. Meanwhile, inorganic compounds, such as pyrophosphates, nitrates and molybdates, are also applied to modify phosphate films. However, most additives are harmful to the environment and human health.

Recently, the application of metal oxide particles in biomedical and environmental materials has attracted great interest due to their advantages in their comprehensive performance and environmental friendliness [17-19]. As reported [20-24], the addition of metal oxide particles, such as  $\text{TiO}_2$ ,  $\text{ZnO}$  and  $\text{ZrO}_2$ , can improve the mechanical properties and protective properties of the conversion coating on metal surface. However, there are few reports on the improvement of the protective performance of the phosphate film through metal oxide particle doping. In particular, few studies on the addition of  $\text{Bi}_2\text{O}_3$  particles have been reported. Bismuth oxide has attracted great attention in recent years due to its photocatalytic performance.  $\text{Bi}_2\text{O}_3$  is a kind of functional metal oxide semiconductor with unique physicochemical properties, such as nontoxicity, high oxygen-ion conductivity, high dielectric permittivity, high refractivity, remarkable photoconductivity and photocatalytic activity [25-28].  $\text{Bi}_2\text{O}_3$  materials can degrade different kinds of pollutants when exposed to sunlight. Chen [29] studied the photocatalytic performance of a graphene oxide/ $\text{TiO}_2$ - $\text{Bi}_2\text{O}_3$  hybrid coating for organic dyes and NO gas. The organic dyes are oxidized to  $\text{CO}_2$  and  $\text{H}_2\text{O}$ , while the NO can be removed by eventually forming  $\text{NO}_3^-$ .

In this work, a multifunctional  $\text{Bi}_2\text{O}_3$ /phosphate composite film with both good corrosion resistance and photocatalytic activity was prepared on AZ91D magnesium alloy by a phosphate treatment. The photocatalytic activity of the composite phosphate film was designed to give the Mg alloy the ability to remove pollutants accumulated on its surface, which could provide magnesium alloy with extra protection. Furthermore, this property might contribute to environmental protection. The photocatalytic performance of the composite film was examined by the photocatalytic degradation of Congo Red. The mechanism of modification with  $\text{Bi}_2\text{O}_3$  particles was also discussed in detail.

## 2. EXPERIMENTAL PROCEDURE

### 2.1 Materials and treatment process

The experimental material used for this investigation was die-casting AZ91D magnesium alloy (7 mm × 7 mm × 30 mm) with a nominal composition (wt %) of 9% Al, 1% Zn and Mg balance. Before treatment, the Mg substrates were carefully polished with 2000-grit SiC paper, rinsed with deionized water and alcohol, and then dried in cold air.

A composite film was prepared on the magnesium alloy AZ91D through two steps. At first, the substrates were immersed in the phosphating treatment solution for 5 min. The treatment solution was composed of calcium nitrate and ammonium dihydrogen phosphate (25 g/L  $\text{Ca}(\text{NO}_3)_2 \cdot 4\text{H}_2\text{O}$  and 15 g/L  $\text{NH}_4\text{H}_2\text{PO}_4$ , respectively). Then, a set amount of  $\text{Bi}_2\text{O}_3$  (5 g/L) was added to the treatment solution. Ultrasonic agitation was applied to disperse the  $\text{Bi}_2\text{O}_3$  particles evenly in the treatment solution. The solution temperature was maintained at 25°C throughout the experiment. A composite phosphate film was prepared on the AZ91D Mg alloy after further immersion in the  $\text{Bi}_2\text{O}_3$ -containing phosphating bath for 40 min.

### 2.2 Characterization of $\text{Bi}_2\text{O}_3$ /phosphate composite film

The contact angle measurements on bare Mg alloy AZ91D and the phosphate-treated samples were conducted using a video contact angle tester JY-82 under ambient atmospheric conditions to determine the wettability of the film. The phase compositions of the composite film were identified by a X-ray diffractometer (XRD, D8, Germany) within the range of  $2\theta = 10 - 80^\circ$ . The surface morphologies of the composite phosphate film were observed by scanning electron microscopy (SEM, JSM-5510LV, Japan) at 20 kV. The film thickness was estimated from the cross-sectional SEM image. The compositions of the film prepared on the AZ91D samples were determined by energy-dispersive X-ray (EDX) analysis. X-ray photoelectron spectroscopy (XPS) measurements were carried out on a Thermo Fisher Scientific Escalab 250Xi to further confirm the compositions of the film. All measurements were taken at the center of the coated samples.

### 2.3 Electrochemical measurements

The corrosion resistance of the composite film-coated samples were estimated by potentiodynamic polarization curve and electrochemical impedance spectroscopy (EIS) measurements. Electrochemical tests were carried out using a classical three-electrode cell with platinum as the counter electrode, a saturated calomel electrode (SCE) as the reference electrode, and the treated AZ91D as the working electrode. All electrochemical measurements were performed in an ASTM D1384-87 solution containing 148 mg/L (1.04 mM)  $\text{Na}_2\text{SO}_4$  + 138 mg/L (1.64 mM)  $\text{NaHCO}_3$  + 165 mg/L (2.82 mM)  $\text{NaCl}$ , which was made up from analytical grade reagents and deionized water. The pH of the solution was 8.2. The potentiodynamic curves were obtained using an electrochemical analyzer (CS 310, China) from -100 mV to 100 mV vs open circuit potential (OCP) at a constant voltage scanning rate of 0.5 mV/s. EIS

measurements were conducted over a frequency range of 100 kHz to 10 mHz with a sinusoidal amplitude of 10 mV. Prior to each electrochemical test, a stabilization period of 1800 s was applied. All electrochemical measurements were performed at room temperature. The composite film-coated sample was immersed for 7 days to estimate the durability of the composite film.

#### 2.4 Photocatalytic activity test

In this study, Congo Red was chosen as the substrate for the photocatalytic activity test to estimate the photocatalytic performance of the  $\text{Bi}_2\text{O}_3$ /phosphate composite film. The test was conducted under natural sunlight at room temperature to examine the practical photocatalytic performance. A  $\text{Bi}_2\text{O}_3$ /phosphate composite film-coated sample (7 mm  $\times$  7 mm  $\times$  30 mm) was immersed in 50 mL Congo Red solution (10 mg/L) for 14 days. The concentration of the Congo Red solution was measured by monitoring the absorbance at 497 nm (the maximum absorbance wavelength of Congo Red) using a UV-vis spectrophotometer (UV-3200pc, MAPADA).

### 3. RESULTS AND DISCUSSION

#### 3.1 Characterization of $\text{Bi}_2\text{O}_3$ particles

Figure 1 and Figure 2 show the XRD and SEM characterization of the  $\text{Bi}_2\text{O}_3$  particles, respectively. From the XRD pattern, there are five main peaks visible on the pattern at  $27.5^\circ$ ,  $33^\circ$ ,  $47^\circ$ ,  $52.5^\circ$  and  $55^\circ$ , corresponding to the faces of the  $\text{Bi}_2\text{O}_3$  crystal [30]. The peaks are sharp and the baseline is flat, indicating good crystallinity of  $\text{Bi}_2\text{O}_3$ . The XRD result shows that the  $\text{Bi}_2\text{O}_3$  particles are pure and crystalline. From the SEM image, crystal clusters with a length of approximately 10  $\mu\text{m}$  and width of approximately 700 nm are observed. In addition, there are considerably smaller cubic crystal clusters.

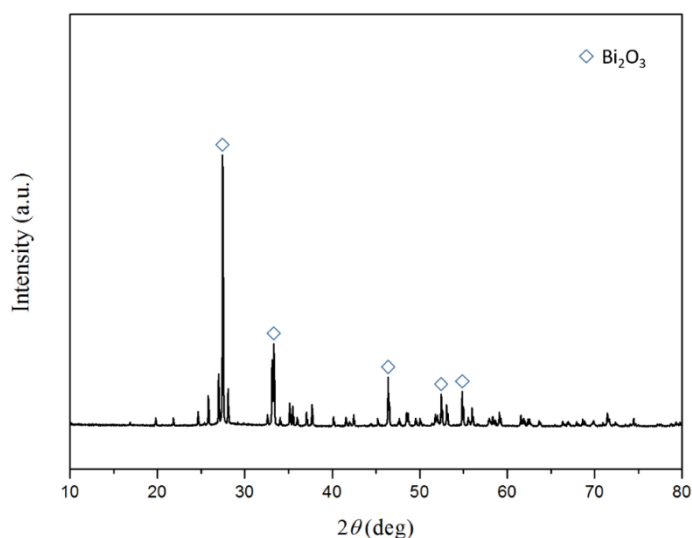


**Figure 1.** XRD pattern of  $\text{Bi}_2\text{O}_3$  particles

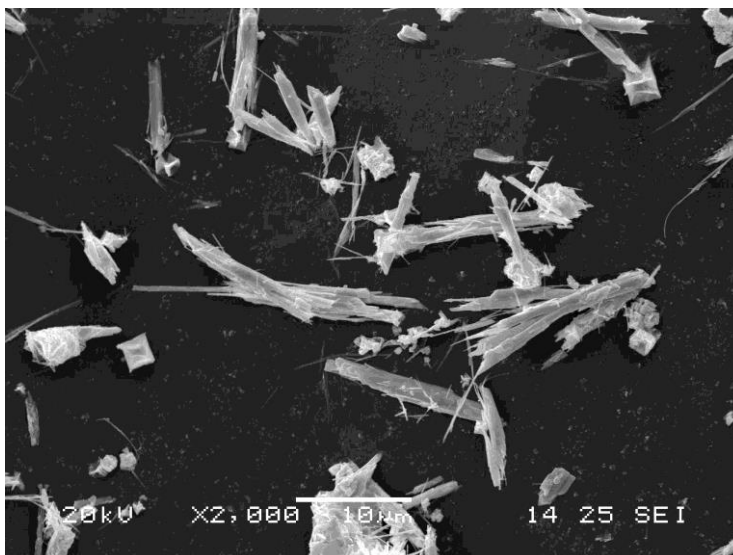


**Figure 2.** SEM image of  $\text{Bi}_2\text{O}_3$  particles

### 3.2 Phase compositions of $\text{Bi}_2\text{O}_3$ /phosphate composite film

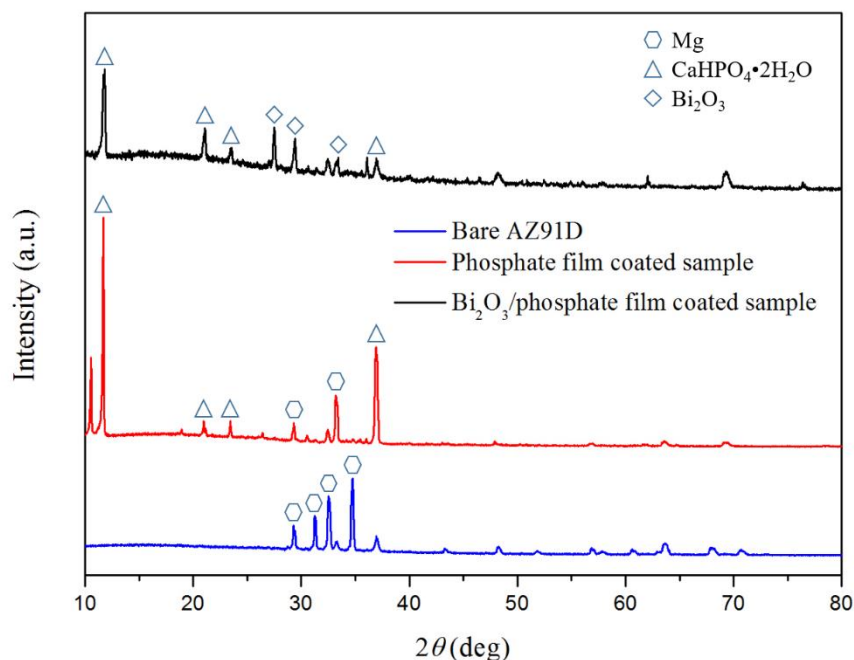


**Figure 3.** XRD patterns of bare AZ91D, phosphate film-coated sample and  $\text{Bi}_2\text{O}_3$ /phosphate composite film-coated sample

X-ray diffraction was employed to identify and investigate the phase compositions of the phosphate film and  $\text{Bi}_2\text{O}_3$ /phosphate composite film. As shown in Figure 3, the obvious difference of the phase compositions between the bare and film-coated samples can be observed. Namely, specific peaks attributed to  $\text{CaHPO}_4$  can be observed in the diffraction pattern of the phosphate film-coated sample, which is consistent with the results of previous research [31]. In the XRD pattern of the  $\text{Bi}_2\text{O}_3$ /phosphate composite film-coated sample, the intensity of the peaks originated from  $\text{CaHPO}_4$  is

lower, while peaks attributed to  $\text{Bi}_2\text{O}_3$  appear, which indicates that the addition of  $\text{Bi}_2\text{O}_3$  particles may affect the crystallinity of  $\text{CaHPO}_4$  and lead to smaller  $\text{CaHPO}_4$  crystals. In addition, peaks attributed to Mg can be observed in the XRD pattern of the phosphate film-coated sample but disappear in the pattern of the  $\text{Bi}_2\text{O}_3$ /phosphate composite film-coated sample, which may indicate that the  $\text{Bi}_2\text{O}_3$ /phosphate composite film is denser than the phosphate film. From these results, crystalline  $\text{CaHPO}_4$  and  $\text{Bi}_2\text{O}_3$  phases coexist in the  $\text{Bi}_2\text{O}_3$ /phosphate composite film.

### 3.3 Morphology and elemental composition of $\text{Bi}_2\text{O}_3$ /phosphate composite film

Figure 4 shows the morphology and elemental composition of the phosphate film-coated sample and  $\text{Bi}_2\text{O}_3$ /phosphate composite film-coated samples prepared with further immersion of 5 min, 10 min and 40 min. From Figure 4(a), it can be seen that the phosphate film mainly consists of Ca, P and O. The atomic ratio of Ca, P and O is approximately 1:1:4. It can be inferred that  $\text{CaHPO}_4$  is the main composition of the film and the  $\text{CaHPO}_4$  crystals seem to be sheet-like [31]. However, the stack of these sheet-like crystals cannot form a compact film and leads to a high interspace rate. The interspace may lead to cracks and severely damage the protective property.

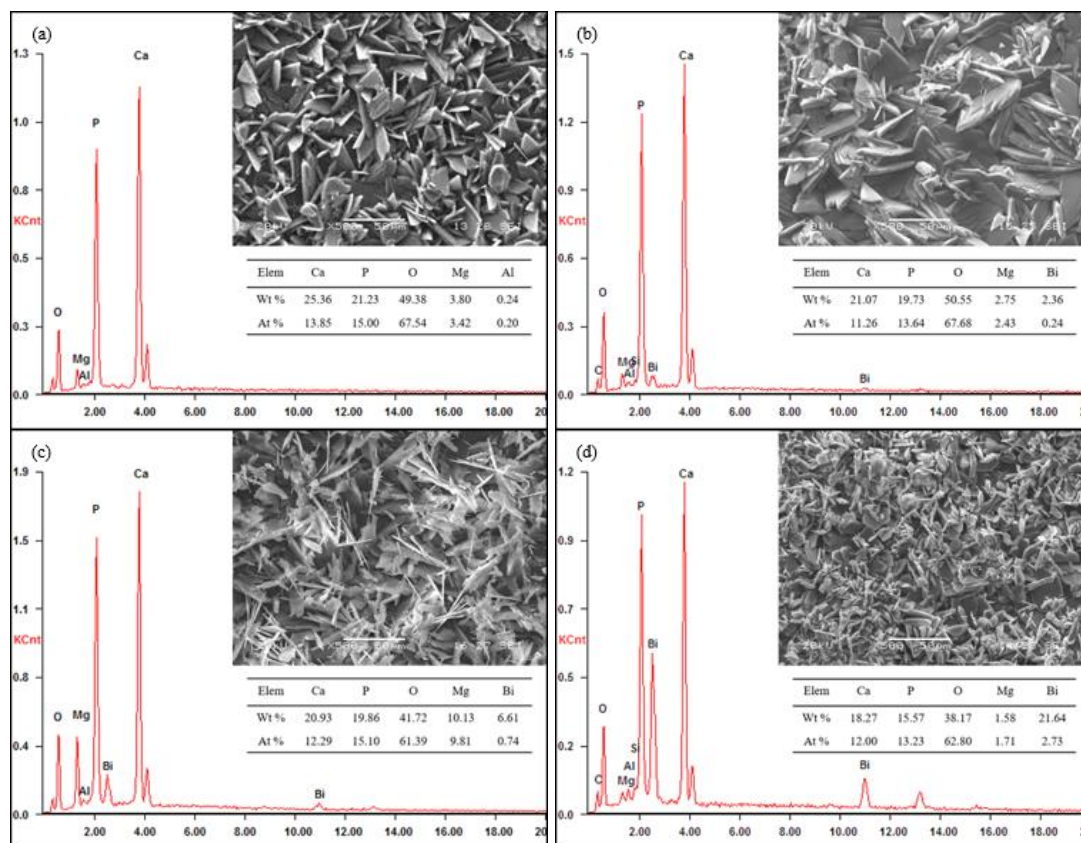


**Figure 4.** SEM images and EDS measurements of  $\text{Bi}_2\text{O}_3$ /phosphate composite film-coated samples prepared with further immersion of (a) 0 min, (b) 5 min, (c) 10 min and (d) 40 min

When the magnesium alloy AZ91D is further immersed in the  $\text{Bi}_2\text{O}_3$ -added system, needle-like crystals gradually appear on the surface of the magnesium alloy, and the atomic ratio of Bi increases

with the extension of further immersion, which indicates the success of the  $\text{Bi}_2\text{O}_3$  doping. The occurrence of these needle-like crystals may be due to the doping of  $\text{Bi}_2\text{O}_3$  particles in the conversion process. It can be seen that the conversion film is composed of tinier crystals after further immersion and the film is more compact.

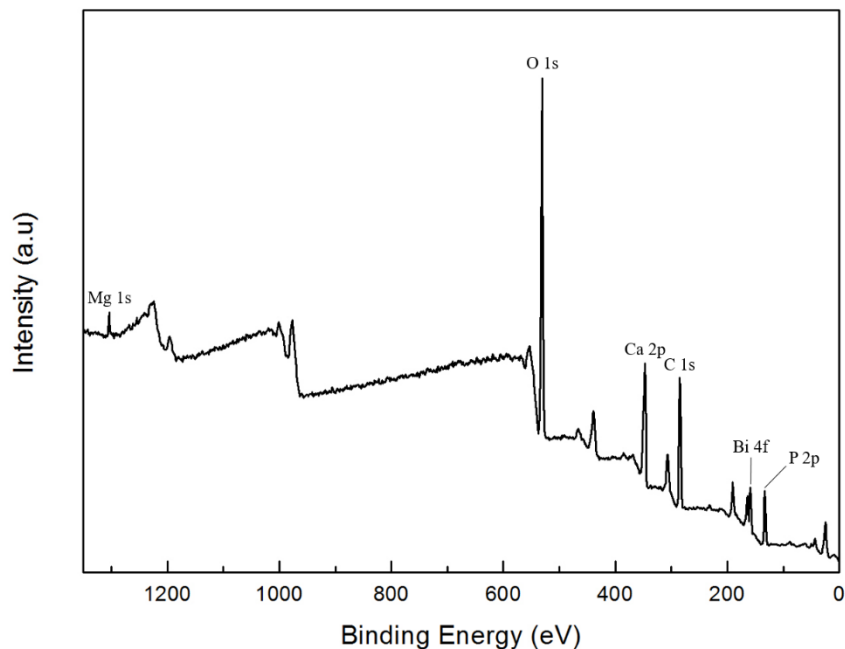


**Figure 5.** XPS analysis of  $\text{Bi}_2\text{O}_3$ /phosphate composite film-coated sample

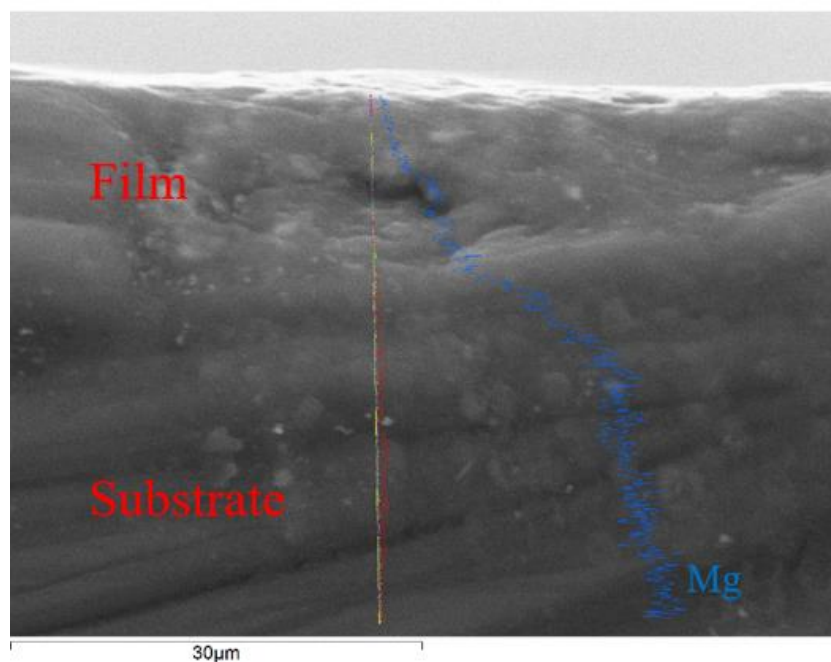


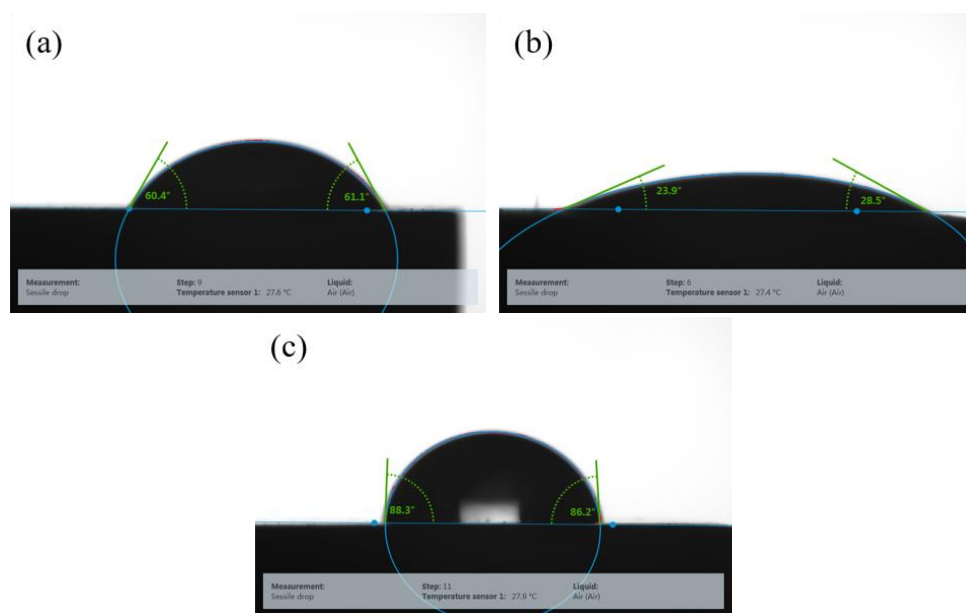
**Figure 6.** Cross-sectional SEM image of  $\text{Bi}_2\text{O}_3$ /phosphate composite film

The elemental composition of the  $\text{Bi}_2\text{O}_3$ /phosphate composite film is further investigated by XPS survey spectra. The wide spectrum demonstrated in Figure 5 provides evidence for the presence of Ca, Bi, P and O, which is consistent with the EDS and XRD results. There are two main peaks visible in the

spectrum at approximately 164.5 eV and 159 eV, corresponding to Bi 4f. Figure 6 shows the cross-sectional SEM image of the  $\text{Bi}_2\text{O}_3$ /phosphate composite film. It can be seen that the composite film is tight and the film thickness is approximately 15  $\mu\text{m}$ .

### 3.4 Contact angle measurements

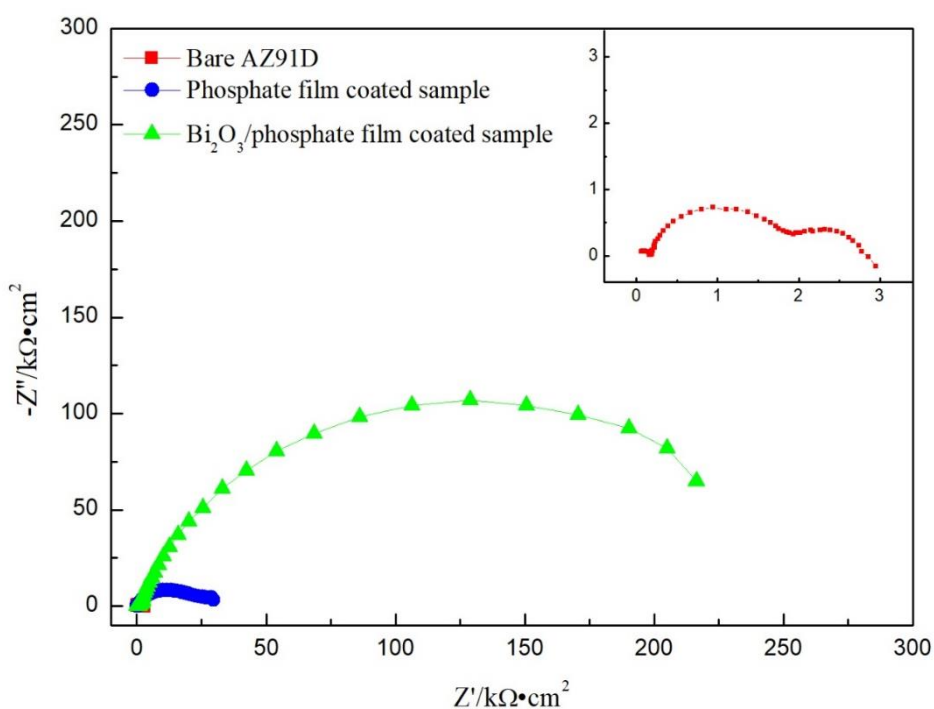
Figure 7 shows the water contact angle measurements on bare AZ91D, phosphate film-coated sample and  $\text{Bi}_2\text{O}_3$ /phosphate composite film-coated sample. The water contact angle measurement is applied to determine the wettability of the modified surface, as well as the tightness and uniformity of the modified layer [32]. If  $\theta < 90^\circ$ , the solid surface is hydrophilic. The smaller the angle is, the better the wettability is. If  $\theta > 90^\circ$ , the solid surface is hydrophobic. The water contact angle on bare AZ91D is approximately  $60^\circ$ , indicating its hydrophilicity. The water contact angles on phosphate film-coated sample and  $\text{Bi}_2\text{O}_3$ /phosphate composite film-coated sample are approximately  $26^\circ$  and  $87^\circ$ , respectively. The difference between these two water contact angle values may be attributed to the different roughness of the two kinds of film, considering that the chemical properties of the two kinds of film should be similar. As discussed above, the phosphate film is composed of thick sheet-like crystals and the surface of the film is notably rough, leading to a small water contact angle. In contrast, the  $\text{Bi}_2\text{O}_3$ /phosphate composite film is composed of thin needle-like crystals and relatively smooth, leading to a larger water contact angle. The water contact angle on the  $\text{Bi}_2\text{O}_3$ /phosphate composite film-coated sample is close to  $90^\circ$ , which means the film is nearly hydrophobic. This property of the composite film could isolate the magnesium substrate from corrosive mediums and provide lasting protection to the magnesium alloy [33].



**Figure 7.** Water contact angles on (a) bare AZ91D, (b) phosphate film-coated sample and (c)  $\text{Bi}_2\text{O}_3$ /phosphate composite film-coated sample

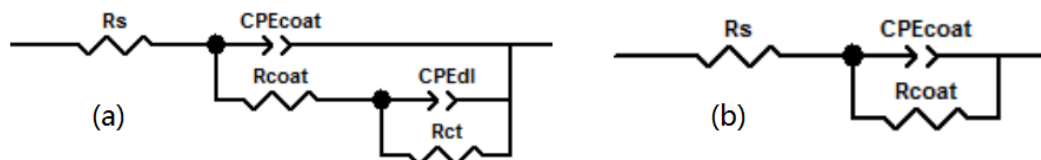
### 3.5 Electrochemical measurements of $\text{Bi}_2\text{O}_3/\text{phosphate}$ composite film-coated sample

Figure 8 shows the EIS of the bare AZ91D alloy, phosphate film-coated sample and  $\text{Bi}_2\text{O}_3/\text{phosphate}$  composite film-coated sample. From Figure 8, the Nyquist plot of the bare AZ91D is composed of two capacitive loops at the tested frequency range, while the Nyquist plots of the phosphate film-coated sample and  $\text{Bi}_2\text{O}_3/\text{phosphate}$  composite film-coated sample are composed of only one capacitive loop respectively. Previous studies indicate that the capacitive loop reflects the impedance characteristic of the metal surface and the electrical double layer on the metal surface [34-36]. It is reported that the high frequency capacitive loop is due to the presence of the phosphate coating on the magnesium alloy surface, and the other loop observed at low frequency is attributed to the occurrence of charge transfer in the electrical double layer [37-39]. The Nyquist plot of the  $\text{Bi}_2\text{O}_3/\text{phosphate}$  composite film-coated sample manifests as a deformed single capacitive loop, indicating that the  $\text{Bi}_2\text{O}_3/\text{phosphate}$  composite film does not participate or produce intermediate products such as adsorption complexes in the electrode reaction. This finding is observed because the attachment of the composite film on the alloy surface will increase the dispersion effect and reduce the capacitance value of the electrical double layer. The disappearance of the other loop at the low frequency range in the Nyquist plots of the phosphate film-coated sample and  $\text{Bi}_2\text{O}_3/\text{phosphate}$  composite film-coated sample may be attributed to the excellent protective effect of the conversion film [40]. As shown in Figure 8, the diameter of the capacitive loop of the  $\text{Bi}_2\text{O}_3/\text{phosphate}$  composite film-coated sample is approximately 8 times larger than that of the phosphate film-coated sample and 100 times larger than that of the bare AZ91D alloy.



**Figure 8.** EIS of the bare AZ91D alloy, phosphate film-coated sample and  $\text{Bi}_2\text{O}_3/\text{phosphate}$  composite film-coated sample

According to the corrosion process and references [41, 42], two equivalent electrical circuits in Figure 9 are presented to fit the EIS results, where  $R_s$  is the solution resistance,  $R_{ct}$  is the charge-transfer resistance and  $R_{coat}$  is the conversion film resistance. The parameters of the fitting results for Figure 8 are listed in Table 1, in which a higher  $R_{coat}$  value represents better corrosion resistance. From Table 1, it can be seen that the  $R_{coat}$  value of the  $Bi_2O_3$ /phosphate composite film-coated sample is much higher than that of the phosphate film-coated sample, indicating the outstanding protective property of the  $Bi_2O_3$ /phosphate composite film.



**Figure 9.** Equivalent electrical circuits used for fitting the impedance data

**Table 1.** Fitting results obtained from Nyquist plots of bare AZ91D and phosphating treated samples

Sample	$R_{coat}(k\Omega \cdot cm^2)$
Bare AZ91D	1.7
Phosphate film-coated sample	20.6
$Bi_2O_3$ /phosphate composite film-coated sample	272.1
After 1 day of immersion	212.6
After 7 days of immersion	91.9

To further confirm the outstanding protective property of the  $Bi_2O_3$ /phosphate composite film, the potentiodynamic polarization curve measurements of the bare magnesium alloy AZ91D, phosphate film-coated sample and  $Bi_2O_3$ /phosphate composite film-coated sample are demonstrated in Figure 10. The corrosion potential ( $E_{corr}$ ), current density ( $j_{corr}$ ) and their corresponding anodic/cathodic Tafel slopes ( $b_a$  and  $b_c$ ) are derived directly from the polarization curves by Tafel region extrapolation, which are listed in Table 2. The  $E_{corr}$  and  $j_{corr}$  of bare AZ91D are  $-1.5325$  V vs SCE and  $4.192 \times 10^{-5}$  A/cm<sup>2</sup>, respectively. Compared with  $E_{corr}$  of the bare AZ91D in Table 2,  $E_{corr}$  of the phosphating treated samples shifts slightly towards a more negative potential. In addition,  $E_{corr}$  of the phosphate film-coated sample is more negative than that of the  $Bi_2O_3$ /phosphate composite film-coated sample. The  $j_{corr}$  of the  $Bi_2O_3$ /phosphate composite film-coated sample significantly decreases by more than 100 times compared to that of the bare AZ91D, which confirms the excellent corrosion resistance of the  $Bi_2O_3$ /phosphate composite film. The corrosion resistance performance is also compared to those

reported by previous studies. Jayaraj [43] studied the protective effect of composite magnesium phosphate coatings on the magnesium AZ31 alloy. The results revealed that the corrosion performance increased with increase in the coating bath pH which could be attributed to the uniform and dense magnesium phosphate coating with fewer defects and increase in the content of insoluble struvite phase. The corrosion current density of the film-coated sample in 1 wt.% NaCl corrosive environment was 16 times lower than that of the bare substrate. Lee [44] prepared a phosphate/permanganate conversion coating with a thickness of 8 μm on AZ31 magnesium alloy. The study found that the  $i_{corr}$  decreased approximately one order of magnitude as the solution permanganate concentration was increased. The corrosion resistance of the composite film-coated magnesium was approximately 5 times stronger than that of the bare substrate in a salt spray test.

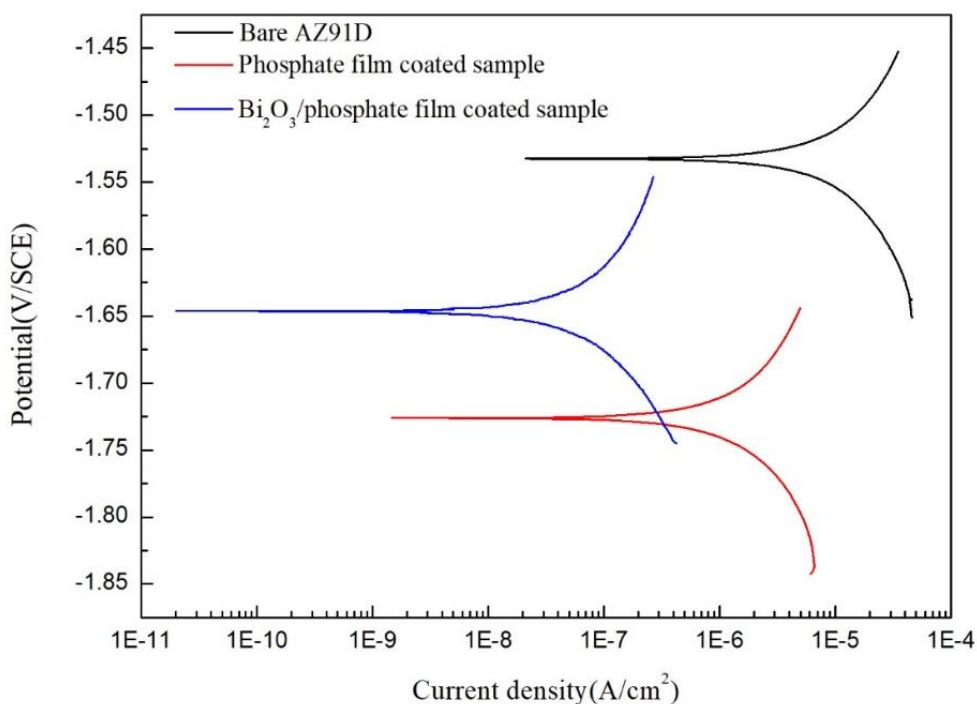


**Figure 10.** Potentiodynamic polarization curves of bare AZ91D, phosphate film-coated sample and Bi<sub>2</sub>O<sub>3</sub>/phosphate composite film-coated sample

**Table 2.** Corrosion parameters obtained by Tafel extrapolation method from polarization curves

Sample	$b_a$ (mV/decade)	$b_c$ (mV/decade)	Corrosion current density(A/cm <sup>2</sup> )	Corrosion potential (V vs SCE)
Bare AZ91D	399.12	-479.11	$4.192 \times 10^{-5}$	-1.5325
phosphate film-coated sample	494.87	-235.30	$6.075 \times 10^{-6}$	-1.7260
Bi <sub>2</sub> O <sub>3</sub> /phosphate composite film-coated sample	196.99	-141.55	$1.083 \times 10^{-7}$	-1.6462

For the application of the  $\text{Bi}_2\text{O}_3$ /phosphate composite film in corrosion protection, it is not sufficient to determine the initial protection level. It is also necessary to verify if the protection remains satisfactory for a long time. For this reason, the  $\text{Bi}_2\text{O}_3$ /phosphate composite film-coated sample (prepared with further immersion of 40 min) was immersed in the ASTM D1384-87 solution for 7 days to estimate the durability of the composite film. Figure 11 shows the EIS of the  $\text{Bi}_2\text{O}_3$ /phosphate composite film-coated sample before the durability test, after immersion of 1 day and after immersion of 7 days. The parameters of the fitting results are listed in Table 1.

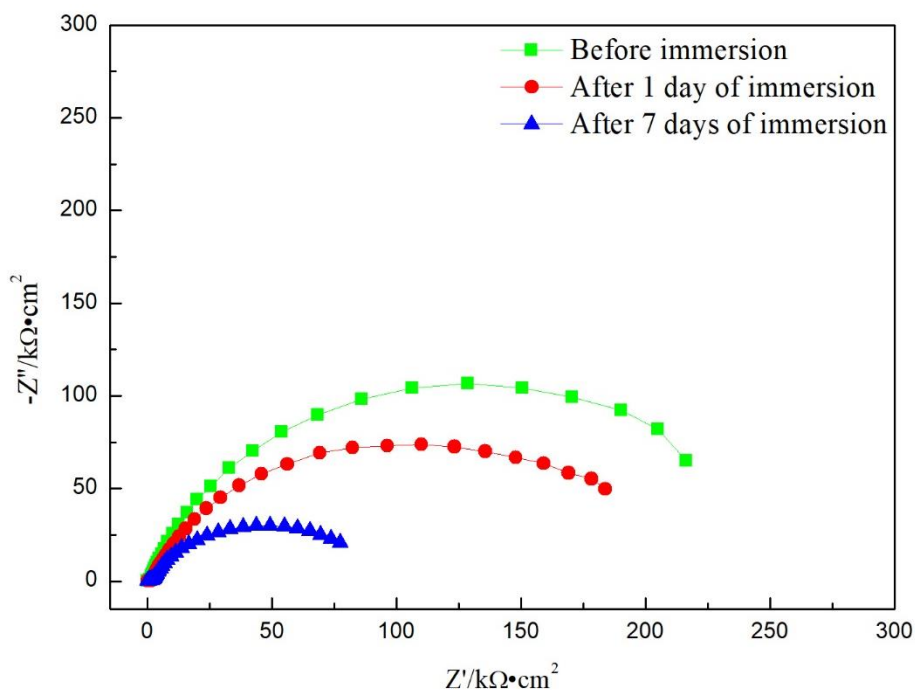
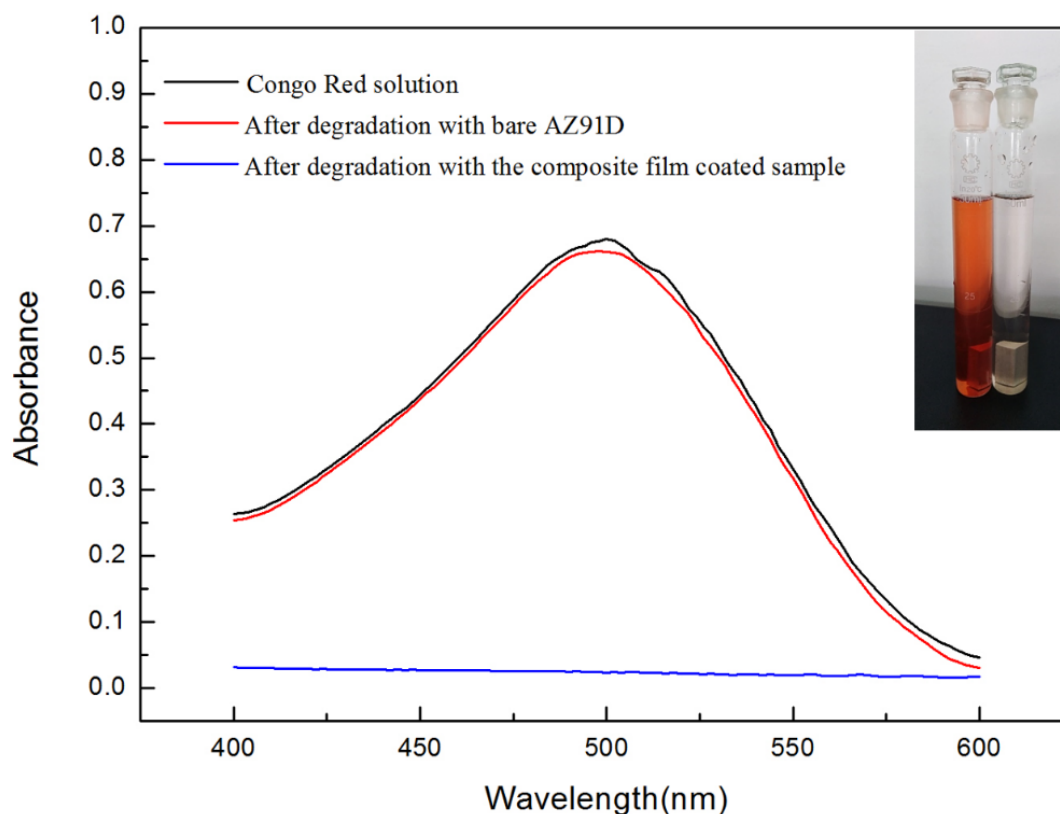


**Figure 11.** EIS of the  $\text{Bi}_2\text{O}_3$ /phosphate composite film-coated sample through the immersion test

From Figure 11, the shape of Nyquist plots of the  $\text{Bi}_2\text{O}_3$ /phosphate composite film-coated sample after immersion of 1 day and after immersion of 7 days does not notably change, which indicates that the structure of the  $\text{Bi}_2\text{O}_3$ /phosphate composite film still remains complete. However, the diameter of capacitive loop reduces, which indicates the resistance of the composite film decreases. The decrease in the resistance of the composite film may be because of the partial dissolution of the composite film. As mentioned above, the film was still hydrophilic after modification with  $\text{Bi}_2\text{O}_3$  particles and the film would slowly dissolve in the corrosive medium. It is mainly ascribed to the fact that the main composition ( $\text{CaHPO}_4$ ) is slightly soluble in water and the  $\text{Cl}^-$  in the corrosive medium may accelerate the dissolution of  $\text{CaHPO}_4$  [45]. The dissolution of  $\text{CaHPO}_4$  will make the composite film thinner. Thus, the resistance of the composite film decreases. However, the resistance value of the composite film is still much higher than that of the phosphate film, which indicates the composite film retains its excellent protective property after immersion. These results demonstrate the durability of the  $\text{Bi}_2\text{O}_3$ /phosphate composite film.

### 3.6 Photocatalytic performance of the Bi<sub>2</sub>O<sub>3</sub>/phosphate composite film-coated sample

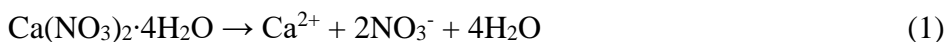
As shown in Figure 12, the Congo Red solution became colorless after 14 days of degradation under sunlight with the Bi<sub>2</sub>O<sub>3</sub>/phosphate composite film-coated sample, while the Congo Red solution of the blank group remained almost unchanged. Combined with the absorption curves of the blank group and the experimental group, the absorbance of the Congo Red solution of the blank group remained the same after 14 days, suggesting that Congo Red was quite stable under sunlight. In contrast, the absorbance of the Congo Red solution after 14 days of degradation with the Bi<sub>2</sub>O<sub>3</sub>/phosphate composite film-coated sample almost became zero, which indicated that the Congo Red had been degraded completely. The above results show the satisfying photocatalytic performance of the Bi<sub>2</sub>O<sub>3</sub>/phosphate composite film. Considering that studies on the photocatalytic degradation of various substrates with Bi<sub>2</sub>O<sub>3</sub> have been reported [46-50], the Bi<sub>2</sub>O<sub>3</sub>/phosphate composite film should be able to degrade different kinds of pollutants. This property of the composite film can protect Mg alloy from corrosion by atmospheric pollutants.

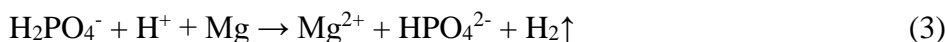


**Figure 12.** Photocatalytic performance of the Bi<sub>2</sub>O<sub>3</sub>/phosphate composite film-coated sample

### 3.7 Mechanism

The formation mechanism of the phosphate film on the AZ91D magnesium alloy is demonstrated in Figure 13. The main composition of the film (CaHPO<sub>4</sub>) forms by the following reactions:





At the beginning, the surface of the AZ91D alloy occurs the dissolution of Mg substrate and hydrogen evolution because the phosphating treatment solution is acidic (pH=2.8), resulting in the generation of  $\text{Mg}^{2+}$  and the elevation of local pH near the surface of AZ91D alloy. The elevation of local pH promotes the further ionization of  $\text{H}_2\text{PO}_4^-$  ion.  $\text{H}_2\text{PO}_4^-$  ion ionizes to produce  $\text{HPO}_4^{2-}$  ion and  $\text{H}^+$ . When the product of the  $\text{Ca}^{2+}$  and  $\text{HPO}_4^{2-}$  concentrations ( $[\text{Ca}^{2+}] \times [\text{HPO}_4^{2-}]$ ) reaches the solubility product ( $K_{\text{sp}}$ ),  $\text{CaHPO}_4$  precipitates on the surface of the magnesium alloy. Hence, the sheet-like  $\text{CaHPO}_4$  crystals deposit on the Mg alloy surface after immersion in the phosphating bath, providing AZ91D alloy with protection verified by electrochemical results. However, as shown in Figure 4(a), the  $\text{CaHPO}_4$  crystals are of relatively large size and simply stack together, which leaves considerable interspace and numerous defects between the crystals. Undoubtedly, this would make the phosphate film porous and thus lower its protective effect in a corrosive environment.

At this point, the introduction of  $\text{Bi}_2\text{O}_3$  particles into the phosphating treatment solution for further immersion plays a crucial role in the remarkable improvement of the corrosion resistance of the phosphate film. This finding can be ascribed to the following two reasons. For one thing, the addition of  $\text{Bi}_2\text{O}_3$  particles obviously affects the crystallinity of  $\text{CaHPO}_4$ , which reduces the size of the  $\text{CaHPO}_4$  crystals. Predictably, the smaller  $\text{CaHPO}_4$  crystals stack together with less interspace and thus form a more compact layer of film, providing the magnesium alloy with greater protection. For another, the  $\text{Bi}_2\text{O}_3$  particles with smaller sizes can fill the interspace between the  $\text{CaHPO}_4$  crystals, which fixes the defects of the phosphate film and makes the film complete. The cross-sectional SEM image verifies the intactness of the  $\text{Bi}_2\text{O}_3$ /phosphate composite film. With no doubt, such an intact layer of conversion film can play a role as a barrier better, hindering the contact between the corrosive medium and Mg substrate, which significantly improves the protective effect of the composite film. Therefore, both the EIS and polarization curves shown in Figure 8 and Figure 10 indicate the remarkable increase in corrosion resistance of the composite film. In fact, the decrease in size of the  $\text{CaHPO}_4$  crystals and repair of the interspace between  $\text{CaHPO}_4$  crystals are closely associated with the introduction of  $\text{Bi}_2\text{O}_3$  particles, which is called “blocking effect” in this paper. The blocking effect is described in detail: when the magnesium alloy sample was further immersed in the  $\text{Bi}_2\text{O}_3$ -added phosphating treatment solution, the  $\text{Bi}_2\text{O}_3$  particles were adsorbed on the surface of growing  $\text{CaHPO}_4$  crystals because of the porosity of the phosphate film, which blocks their further growth in crystal size and thus leads to the formation of smaller  $\text{CaHPO}_4$  crystal clusters with the inclusion of  $\text{Bi}_2\text{O}_3$ . The SEM images in Figure 4 are the best proof, in which with the extension of further immersion, the small-size  $\text{CaHPO}_4$  crystals begin to appear and the proportion of small-size  $\text{CaHPO}_4$  crystal cluster gradually increases, while the  $\text{Bi}_2\text{O}_3$  particles also gradually fill the interspace. All the EDS, XRD and XPS results confirm the presence of  $\text{Bi}_2\text{O}_3$  in the composite film. In addition, the content of  $\text{Bi}_2\text{O}_3$  in the composite film increases with the prolongation of immersion, which indicates the lasting blocking effect improves the compactness and corrosion resistance of the composite film in the chemical conversion process. Interestingly, the composite film not only possesses high corrosion resistance but also possesses the additional photocatalytic activity. This means that the  $\text{Bi}_2\text{O}_3$ /phosphate composite film can protect the Mg substrate

from corrosion while this film can degrade some pollutants as discussed in section 3.6, which is friendly to the environment and attractive in practical applications.

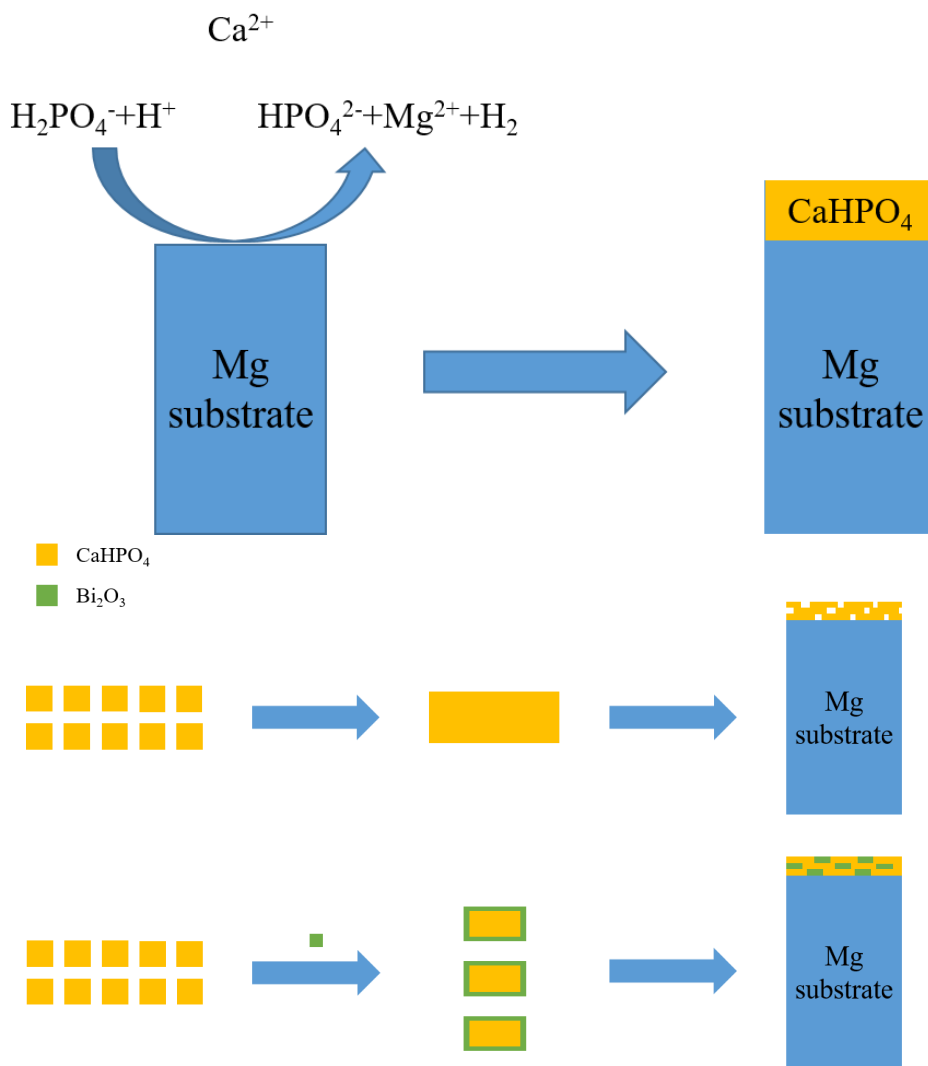


**Figure 13.** Formation mechanism of phosphate film on AZ91D magnesium alloy

#### 4. CONCLUSIONS

A Bi<sub>2</sub>O<sub>3</sub>/phosphate composite film was prepared on AZ91D magnesium alloy by phosphating. The film was composed of small crystal clusters and the surface of the film was relatively smooth. The modification with Bi<sub>2</sub>O<sub>3</sub> particles made the film tight and complete. The film thickness was estimated to be approximately 15 μm and the composite film was primarily composed of CaHPO<sub>4</sub> and Bi<sub>2</sub>O<sub>3</sub>. The composite film-coated AZ91D showed excellent corrosion resistance. The durability of the composite film-coated sample was also investigated by an immersion test. The composite film still possessed a satisfactory protective effect after immersion in the ASTM D1384-87 solution for 7 days. Furthermore, the composite film possessed good photocatalytic activity.

## ACKNOWLEDGEMENTS

The work was supported by the Open Research Fund of the State Key Laboratory of Oil, Gas Reservoir Geology and Exploitation (No.PLN1115), the Key Project of the Chinese Ministry of Education (No.213024A) and the China National Natural Science Foundation (No.51601133, No.51574182, No.51401150).

## References

1. F. Liu, D. Shan, Y. Song, E.H. Han, W. Ke, *Corros. Sci.*, 53 (2011) 3845.
2. E. Rocca, C. Juers, J. Steinmetz, *Corros. Sci.*, 52 (2010) 2172.
3. W. Jiang, X. Chen, B. Wang, Z. Fan, H. Wu, *Int. J. Adv. Manuf. Tech.*, 83 (2016) 1.
4. Z. She, Q. Li, Z. Wang, L. Li, F. Chen, J. Zhou, *ACS Appl. Mater. Inter.*, 4 (2012) 4348.
5. W. Zhou, D. Shan, E.H. Han, W. Ke, *Corros. Sci.*, 50 (2008) 329.
6. H. Huang, Z. Pan, Y. Qiu, X. Guo, *MiRe*, 53 (2013) 1149.
7. H.Y. Su, C.S. Lin, *Corros. Sci.*, 83 (2014) 137.
8. X. Ding, L.F. Xue, X.C. Wang, K.H. Ding, S.L. Cui, Y.C. Sun, M.S. Li, *J. Magn. Magn. Mater.*, 416 (2016) 247.
9. L.Y. Niu, Z.H. Jiang, G.Y. Li, C.D. Gu, J.S. Lian, *Surf. Coat. Tech.*, 200 (2006) 3021.
10. L. Kouisni, M. Azzi, M. Zertoubi, F. Dalard, S. Maximovitch, *Surf. Coat. Tech.*, 185 (2004) 58.
11. L. Kouisni, M. Azzi, F. Dalard, S. Maximovitch, *Surf. Coat. Tech.*, 192 (2005) 239.
12. R. Amini, A.A. Sarabi, *Appl. Surf. Sci.*, 257 (2011) 7134.
13. Q. Li, S. Xu, J. Hu, S. Zhang, X. Zhong, X. Yang, *Electrochim. Acta*, 55 (2010) 887.
14. E. Gomez, M. Fillit, M.C. Ximenes, B. Picot, *Hydrobiologia*, 373-374 (1998) 203.
15. R. Zeng, Z. Lan, L. Kong, Y. Huang, H. Cui, *Surf. Coat. Tech.*, 205 (2011) 3347.
16. Z. Yong, Z. Jin, Q. Cheng, Y. Liu, *Appl. Surf. Sci.*, 255 (2008) 1672.
17. C. Wei, W. Lu, H. Xu, *Nano Today*, 10 (2015) 717.
18. J. Xiong, G. Cheng, F. Qin, R. Wang, H. Sun, R. Chen, *Chem. Eng. J.*, 220 (2013) 228.
19. Y. Gan, Y. Wei, J. Xiong, G. Cheng, *Chem. Eng. J.*, (2018).
20. J. Wang, Y.Q. Wu, S. Zhang, *Stud. Conserv.*, 59 (2014) 268.
21. R.U. Din, V.C. Gudla, M.S. Jellesen, R. Ambat, *Surf. Coat. Tech.*, 296 (2016) 1.
22. E. Klyatskina, E. Rayón, G. Darut, M.D. Salvador, E. Sánchez, G. Montavon, *Surf. Coat. Tech.*, 278 (2015) 25.
23. S. Shen, Y. Zuo, *Corros. Sci.*, 87 (2014) 167.
24. Z. Han, Y. Zuo, P. Ju, Y. Tang, X. Zhao, J. Tang, *Surf. Coat. Tech.*, 206 (2012) 3264.
25. T. Saison, N. Chemin, C. Chanéac, O. Durupthy, V. Ruaux, L. Mariey, F. Maugé, P. Beaunier, J.P. Jolivet, *J.phys.chem.c*, 115 (2011) 5657.
26. H. Abdul, M. Tiziano, G. Valentina, F. Paolo, *JACS*, 130 (2008) 9658.
27. Y. Xie, L. Mo, D. Su, M.F. Woldekidan, S. Wu, *J. Hazard. Mater.*, 280 (2014) 260.
28. N.S. Azhar, M.F.M. Taib, O.H. Hassan, M.Z.A. Yahya, A.M.M. Ali, *Mater. Res. Express*, 4 (2017).
29. C. Chen, S. Cao, H. Long, G. Qian, Y. Tsang, L. Gong, W. Yu, Y. Xiao, *J. Mater. Sci-Mater. El.*, 26 (2015) 3385.
30. O. Monnereau, L. Tortet, P. Llewellyn, F. Rouquerol, G. Vacquier, *Solid State Ionics*, 157 (2003) 163.
31. D. Liu, Y. Li, Y. Zhou, Y. Ding, *Materials*, 11 (2018).
32. E.K. Mioč, Z.H. Gretić, H.O. Čurković, *Corros. Sci.*, (2018).
33. W. Li, L. Zhu, H. Liu, *Surf. Coat. Tech.*, 201 (2006) 2573.
34. M. Mouanga, M. Puiggali, O. Devos, *Electrochim. Acta*, 106 (2013) 82.
35. A.M. Fekry, M.Z. Fatayerji, *Electrochim. Acta*, 54 (2009) 6522.

36. X.P. Guo, Y. Tomoe, *Corros. Sci.*, 41 (1999) 1391.
37. G.A. Zhang, D. Liu, Y.Z. Li, X.P. Guo, *Corros. Sci.*, 120 (2017) 107.
38. F.F. Eliyan, A. Alfantazi, *J. Mater. Eng. Perform.*, 23 (2014) 4082.
39. H. Huang, T. Jing, *MiRe*, 78 (2017) 131.
40. L. Chang, L. Tian, W. Liu, X. Duan, *Corros. Sci.*, 72 (2013) 118.
41. W. Liu, F. Cao, A. Chen, L. Chang, J. Zhang, C. Cao, *Corros. Sci.*, 52 (2010) 627.
42. L.Y. Cui, S.D. Gao, P.P. Li, R.C. Zeng, F. Zhang, S.Q. Li, E.H. Han, *Corros. Sci.*, 118 (2017) 84.
43. J. Jayaraj, S.A. Raj, A. Srinivasan, S. Ananthakumar, U.T.S. Pillai, N.G.K. Dhaipule, U.K. Mudali, *Corros. Sci.*, 113 (2016) 104.
44. Y.L. Lee, Y.R. Chu, W.C. Li, C.S. Lin, *Corros. Sci.*, 70 (2013) 74.
45. G. Song, A. Atrens, D.S. John, X. Wu, J. Nairn, *Corros. Sci.*, 39 (1997) 1981.
46. G. Zhu, Y. Liu, M. Hojamberdiev, J. Han, J. Rodríguez, S.A. Bilmes, L. Peng, *New J. Chem.*, 39 (2015) 9557.
47. S. Chen, H. Nan, X. Zhang, Y. Yan, Z. Zhou, Y. Zhang, K. Wang, *J. Mater. Chem. B*, 5 (2017) 3718.
48. J. Ke, J. Liu, H. Sun, H. Zhang, X. Duan, P. Liang, X. Li, M.O. Tade, S. Liu, S. Wang, *Appl. Catal. B-Environ.*, 200 (2017) 47.
49. Y. Li, Z. Zhang, Y. Zhang, X. Sun, J. Zhang, C. Wang, Z. Peng, H. Si, *Ceram. Int.*, 40 (2014) 13275.
50. M. Ge, Y. Li, L. Liu, Z. Zhou, W. Chen, *J. Phys. Chem. C*, 115 (2011) 5220.

© 2019 The Authors. Published by ESG ([www.electrochemsci.org](http://www.electrochemsci.org)). This article is an open access article distributed under the terms and conditions of the Creative Commons Attribution license (<http://creativecommons.org/licenses/by/4.0/>).